IEEE Access
Multidisciplinary | Rapid Review | Open Access Journal

Received 4 August 2022, accepted 7 September 2022, date of publication 15 September 2022,
date of current version 26 September 2022.

Digital Object Identifier 10.1109/ACCESS.2022.3206914

RESEARCH ARTICLE

An Optimum Design of Paired Balanced Antipodal Vivaldi Antennas With Mirror-Imaged Symmetric Architectures for Ultra-Broadband Characteristics From Microwave to Millimeter-Wave Frequency Ranges

HSI-TSENG CHOU, (Fellow, IEEE), AND YEN-JU LIN
Graduate Institute of Communication Engineering, National Taiwan University, Taipei 10617, Taiwan

Corresponding author: Hsi-Tseng Chou (chouht@ntu.edu.tw)

This work was supported in part by the National Science and Technology Council, Taiwan; and in part by Qualcomm Corporation Inc., USA.

ABSTRACT This paper presents a balanced antipodal Vivaldi antenna design to produce ultra-broadband radiations from microwave to millimeter-wave frequencies. In particular, this work relaxes the design constraints to optimize the geometrical parameters to broaden the operational frequency bandwidth, where 147% relative bandwidth has been achieved. Moreover, in this optimized design, the beam squint and cross-polarization (X-pol) discrepancy at high frequencies are improved by pairing two mirror-imaged antenna structures to form an integrated one. The resulted X-pol level can retain good performance in the entire band. The beam squint can be minimized by taking advantage of the 3dB gain increase provided by the array factor. HFSS full-wave simulations first examine the proposed work, further validated by measurement from a basic antenna prototype. The beam squint is less than 3 degrees in the major middle part of the achieved band, and the X-pol level is less than -30dB for the paired antennas.

INDEX TERMS Antenna radiation, balanced antipodal Vivaldi antenna, millimeter-wave frequency, ultra-broadband operation.

I. INTRODUCTION

Wireless communications ranging from microwave to millimeter-wave (mmW) frequencies are booming in various civilian applications, which require broad bandwidths. Typical examples include 5G FR2 applications [1], low earth orbit (LEO) satellite communications [2], vehicular advanced driver assistance system (ADAS) [3], wireless gigabit (WiGig) data transmission, wireless local area network (WLAN)based on IEEE 802.11aj, hand-gesture detection, bio-detection and imaging [4], and microwave links. Table 1 summarizes the frequency bands for the applications mentioned above, located in the broadband of 17 $\sim$ 86 GHz.

TABLE 1. Summaries of frequency bands for various applications.

App.	LEO Sate.	5G FR2	ADAS	WiGig	WLAN	Hand Gesture	Bio Imag.	Micro. Link.
Freq.	17-31	28, 39	24, 27	57	45	60	60	71,81

Such applications may be integrated into a single device with different combinations.

It is desirable to develop a single antenna set to accommodate these frequency bands to simplify system implementation cost simultaneously. It is challenging to retain good radiation characteristics in such broad bandwidth and create broadband reflection coefficients. In this case, antipodal Vivaldi antennas (AVA) [5] were considered a good candidate for wide frequency bandwidths. Various efforts have been dedicated to improving radiation characteristics, where

The associate editor coordinating the review of this manuscript and approving it for publication was Chinmoy Saha.

most works were performed at relatively low frequencies. For example, [6], [7] proposed a balanced AVA (BAVA) at 1-18 GHz to improve the cross-polarization levels (XPLs) and the radiation pattern symmetry on the H-plane which results in beam squints on the E-plane at high frequencies. The XPLs also increase with frequencies. Also, [8] proposed to elongate and shape the substrates of BAVA beyond the aperture to increase the gains at 6-20GHz, and improve the high-frequency beam squints.

On the other hand, [9] and [10] employed dielectric or metal directors to increase the radiation directivity at 2.4-18 and 1.5-15 GHz, respectively. Also, [11] used a half-elliptical lens to improve the directivity pattern on the E-plane at 3-18 GHz and beam squints at 12-18 GHz. These works presented various design equations for the AVA metal flares, and most were implemented at low frequencies to solve some particular problems. Several other related works are referred to [12] for a global overview of BAVAs in [13], [14], [15], and [16], such as increasing the front-to-back ratio and creating notches.

The authors' research team recently proposed an asymmetric BAVA structure [17] to improve the E-plane radiations pattern by reducing beam squints over a wide bandwidth by cutting substrate between the metal radiating flare out at 10-40 GHz. It improved the sidelobe levels (SLLs) [18] and XPLs by implementing dual-scale slotted edges to reduce diffraction interferences. The bandwidth performance of 10-40 GHz was achieved by implementing a broadband strip-to-microstrip transition [19], [20] to feed the BAVA structures. This design essentially integrates the specific measures in the past works to improve the radiation performance. The insufficiencies of the work in [17] include the insufficient bandwidth to cover the desired application bands of 17-86 GHz and the unexplored radiation behaviors at the high-frequency bands. It is noted that the selected upper-frequency range in this paper is up to 80 GHz, where the radiating structures may not be confined to the metal flares, as focused by the previous works. Indeed, the feeding structures significantly influence radiation characteristics and distort the symmetric structures established on the metal radiating flares.

In this paper, the structural constraints in [17] are relaxed and optimized to achieve a broad frequency bandwidth, as required by the integrated applications mentioned in Table 1. To minimize the XPLs and beam squints, an antenna pair with mirror-imaged structures [21] is constructed to achieve two goals. First, a second level's symmetric structure ensures a proper X-pol components' cancellation for low XPLs in the broadside direction. Secondly, the 3dB directivity increase in the broadside direction will reduce the beam squint impact of the gain drop to the frequency variation. Moreover, the planar, low-profile nature of AVA retains the antenna architecture very compact when they are paired in a parallel configuration.

The remainder of this paper is organized as follows. Section II summarizes the antenna architectures and basic radiation mechanisms. Section III presents the numerical investigations by HFSS full-wave simulations and parametric studies for broadband operations, highlighting the behaviors at the high part of mmW frequencies. The experimental validation is shown in Section IV examines the radiation characteristics, where comparisons to previous related works are also summarized. A short conclusion is presented in Section V.

II. ANTENNA ARCHITECTURE AND RADIATION MECHANISMS

A. BASIC ANTENNA ARCHITECTURE AND OPERATIONAL MECHANISMS

The proposed antenna architecture is illustrated in Fig. 1, where detailed descriptions of operational principles are available in [17]. We focus on the characteristics of high mmW frequency band extension by optimization. The antenna is a sandwiched structure formed by two dielectric substrates to produce three interface layers and implement three metal Vivaldi radiating flares on the interface surfaces. This antenna is in a dipole format with two essential arms (the metal flares) to radiate the electromagnetic (EM) fields from their gap. The goals of low XPLs and broad bandwidth are achieved by using the following mechanisms. First, the dipole arms are formed by a symmetric configuration. In particular, the positive arm, indicated by the red color flare in Fig. 1, is implemented on the middle interface sandwiched by the two dielectric substrates.

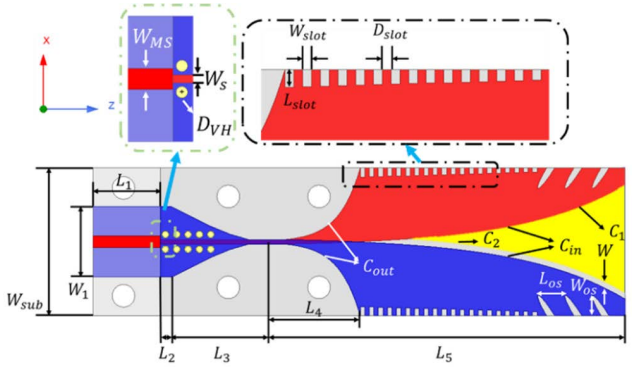

FIGURE 1. Proposed antenna structure and geometrical parameters. The yellow region is the substrate cutout, and the via-hole grounding is also shown.

On the other hand, the opposite arm is split into two parallel ones, indicated by the blue color flares in Fig. 1, which are implemented on the two outer surfaces of the two dielectric substrates. Metal vias short them to form an effective arm. This configuration of dipole arm architecture can minimize the XPLs at low frequencies. The two blue arms can be paired with the red arm to form two dipole sets in a mirror-imaged relationship to the middle interface where the red arm is placed. Thus, the X-pol components polarized along the cross-section dimension of the antenna can be canceled regardless of frequencies to suppress the

XPLs from an EM field vector summation point of view if the radiations are mainly produced from these two arms. To increase radiation efficiency and match the free space impedance, the dielectric substrates on the gap between the two Vivaldi arms are cut out to form the electric lines in free space directly.

On the other hand, the broadband operation is first achieved by modifying the Vivaldi arms' shapes to eliminate the diffraction effects and current flows from the external edges back to the feeding structure. It is further suppressed by cutting slotted edges to suppress the outer edge currents, the return paths back to the feeding structure. Moreover, a broadband microstrip-to-stripline transition is designed. As illustrated in Fig. 1, one dielectric substrate was cut out in this transition such that the microstrip of the red metal flare in this vacant area can be available to be fed by the RF connector. Instead of using a single pair of metal vias in [17], several pairs are implemented by the sides of the stripline for impedance matching [22], which is essential in the current design to produce an ultra-broad bandwidth.

B. MECHANICAL CHALLENGES AND OPTIMIZATION OF THE PROPOSED DESIGN

The work in [17] has achieved a bandwidth of 10-40 GHz, or 120% fractional bandwidth, and is not sufficiently wide to cover the desired frequency band of 17-86 GHz. The physically invariant dimensions of geometric structures result in mechanical limitations [23], [24] at the higher-portions of mmW frequencies to cause radiation discrepancies. Some factors are discussed. First, the dielectric substrates' thickness becomes electrically significant to produce strong EM emissions [25] when the feeding microstrip circuits are implemented. The radiation arises from the metal flares on the portions very close to the feeding transitions, which may cause diffractions to disturb the radiation patterns and produce X-pol components. The substrate cutout in the feeding transition for connector implementation may distort the asymmetric natures of the geometric and feeding structures and reduce the effectiveness of XPL suppression. The mechanical fabrication limitations include the sizes of metal via holes, the separation between adjacent vias, and the microstrip lines' widths on the PCB substrates.

In this paper, the antenna structures are optimized to relax the mechanical limitations and fulfill the design requirements of broadband and low XPLs, especially at the higher frequency portions of mmW frequencies. The basic structures were initiated from work in [17] by extending the geometric parameters, i.e., we increased the optimization freedoms to produce good performances. Several unique treatments on the antenna structure were performed as follows.

1) OPTIMIZING DESIGN EQUATION FOR VIVALDI ARMS

The design equations are optimized to control the radiation patterns and, therefore, the gains because it is challenging to retain a broadband gain performance. The basic equations for the inner and outer curved edge profiles of the copper flares are given by [17]

$$\begin{cases} C_{in} & = \pm[-W_S + (W_S/2)\exp(\alpha_1 z)] \\ C_{out} & = \pm[(W_S/2)\exp(\alpha_2 z)] \end{cases}, \tag{1}$$

where W_S is the width of the feeding stripline at the origin of the copper flares and (α_1, α_2) are indices for controlling the flare's profile. The design criteria are to narrow the opening of the radiating flares for high-frequency radiation control. Thus, the gains at the lower frequency part are slightly smaller than the results in [17] as a compromise of gains and bandwidths.

2) CONSIDERATION OF BROADBAND TAPERED EDGE SLOTS

As illustrated in Fig. 1, the numbers and tapers of edge slots are optimized for a broadband operation from a dual-scale corrugation on the outer edges of the antenna's three copper flares. It is noted that the high-frequency slot widths and their microstrip lines cannot be too small due to the mechanical limitations and the related distortions in fabrication. Thus, to increase the number of high-frequency slots for broadband induced current suppression, the low-frequency slots were reduced from four elements in [17] to three to accommodate twenty high-frequency elements. The slope of the tapered slots is decreased to provide a smoother transition for broadband operation, which is particularly important for the high-frequency induced current suppression. On the other hand, the decrease of low-frequency elements will only slightly affect the radiation patterns, i.e., the symmetry of the E-plane radiation patterns.

In the implementation, the shapes and orientation of the high-frequency slots are rectangular and perpendicular to the edges for easy fabrication, while these low-frequency slots are in pencil shapes and slanted to reduce the depths to the inner edges. These outer edge corrugations are essential for low microwave frequency to middle mmW frequencies for smoother impedance variations.

3) MULTI-VIAS FOR BROAD MATCHING TO FEEDING TRANSITION STRUCTURE

At the higher mmW frequencies, the antenna's radiation arises from the metal flares on the portion near the feeding transition. To achieve broadband matching and avoid EM emissions from the microstrip lines, metal vias are installed to optimize the radiation and reflection coefficients. Full-wave simulations optimize the number of metal vias and their positions to achieve good performance. In this design, five pairs of metal vias are implemented. It is noted that the mechanical fabrication limitations of metal vias-holes should be considered. A metal ring pad should be applied to every vias. They should also be at a distance from the stripline and the junction between the microstrip and stripline. These vias are arranged symmetrically to retain good polarization because the lateral EM leakage produces X-pol fields between the vias and stripline.

4) MIRROR-IMAGED BAVA PAIR FOR LOW XPL AND BEAM SQUINTS

The primary mechanism of the antenna to retain low XPLs of radiations implements mirror-imaged structures to the middle interface between the two dielectric substrates. The structure losses the symmetry on the portion near the feeding port due to the substrate cutout for the connector implementation. The radiation from the feeding structures will produce high XPLs, especially at the high mmW frequencies. To avoid this asymmetric degradation, taking advantage of the antenna's planar low profile, two antennas with mirror-imaged architectures are paired to increase the radiation directivity and suppress the X-pol components, as illustrated in Fig. 2. This paired antenna may increase the directivity by 3dB to reduce the beam squint impact on the antenna gains because of the directional array factor. It also reduced the beam width on the cross-section dimension. In principle, the XPL on the E-plane is zero.

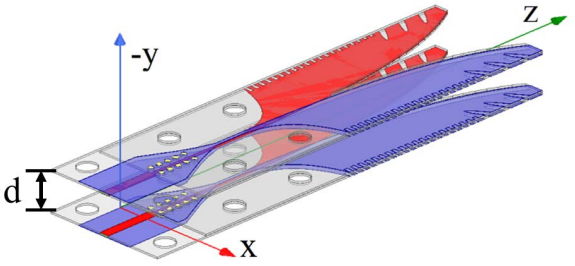

FIGURE 2. A mirror-imaged BAVA pair to reduce XPL and beam squints at high frequencies.

The antenna is realized two RT5880 dielectric substrates, each having 0.254 mm in thickness. The dielectric constant is $\varepsilon_r = 2.2$, and the loss tangent is $tan\,\delta = 0.0009$. The thickness of copper is 0.035mm. The geometric parameters in Fig. 1 are given in Table 2 below after optimizing HFSS full-wave simulations for prototype testing. The feeding is an end-launch connector.

TABLE 2. Optimized values of the single BAVA's geometric parameters labeled in Fig. 1-3 for broadband operations (unit: mm).

L_1	L_2	L_3	L_4	L_5	W_1	S_{VH}	W_{sub}	Y_{VH}
5.936	1	8.5	8.25	31.5	6.2	1	13	0.65
W_{MS}	W_S	W	L_{slot}	W_{slot}	D_{slot}	D_{VH}	D_{VP}	X_{VH}
1.02	0.4	0.55	0.8	0.4	0.4	0.55	0.65	0.45
L_{os}	W_{os}	α_1	α_2					
2.4	1.78	0.11	0.525					

III. FULL-WAVE SIMULATION AND PARAMETRIC STUDIES

One first considers parametric studies by HFSS full-wave simulations to examine the behaviors at high-frequency parts. The studies are based on the optimum parameters in Table 2 to discuss the parametric effectiveness.

A. PARAMETRIC STUDIES

One first examines the multi-via metal structures to build a substrate integrated waveguide (SIW) analogous effectiveness to reduce the EM emissions and produce good impedance matching. Due to the fabrication stability requirement, the diameter of the via holes is 0.55 mm, as shown in Table 2 for good behaviors of reflection coefficients. A metal ring of 0.65 mm in diameter is added to via holes for a complete structure. The parameters under study are the separation distances to the stripline and the junction of the microstrip-to-stripline transition, as illustrated in Fig. 3 (a). One first examines the impedance matching behaviors. The reflection coefficients are shown in Fig. 3(b) and (c), respectively, as expected that these two parameters mainly affect the high-frequency parts. The offset to the transition junction between the microstrip and stripline affects the reflection coefficients at frequencies beyond 48 GHz, while the separation to the stripline affects the behaviors beyond 64 GHz. In particular, when the vias are not used, the reflection coefficients at the lower frequency part will also be affected in addition to the

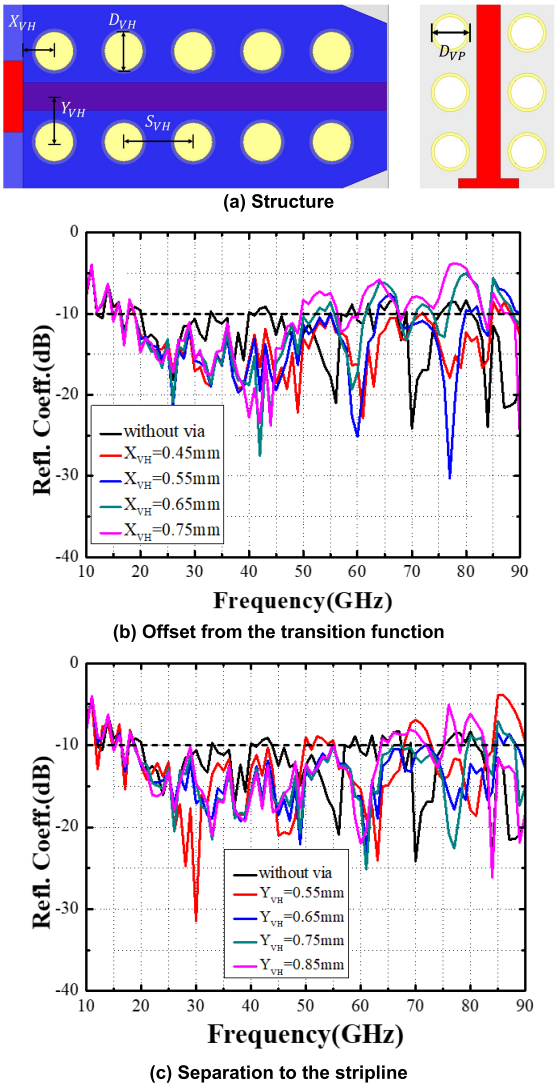

FIGURE 3. Reflection coefficients for parametric studies of separation distances to the stripline and its junction to the microstrip line.

high-frequency parts. The use of metal vias may effectively improve the low-frequency parts. These vias should be placed in the proper positions to assure good performance. When it is too far away from the transition junction, the reflection coefficients at the high-frequency parts will be degraded. However, the shortest distance is limited to the fabrication requirement for stability. Similar phenomena apply to the separation between the vias and the stripline, particularly important for high-frequency parts.

One following examines the effectiveness of the diameter of the metal vias, where the reflection coefficients are shown in Fig. 4. It is seen that this parameter also affects the high-frequency behaviors beyond 60 GHz. In general, a smaller one produces better results. However, this is not a certain rule because minor deviation may happen. Optimization should be performed.

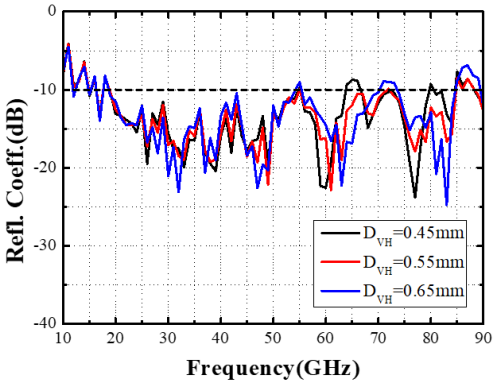

FIGURE 4. Reflection coefficients for parametric studies of D_{VH}.

One also considers an important factor in altering the radiation patterns, especially the main beam pattern forming to result in beam squints to frequencies, which is the width of the dielectric substrate leftover after the dielectric substrate cutout in Fig. 1. Fig. 5 (a) illustrates the width of the leftover dielectric substrate on the side of the twin blue flares. This leftover was intended to balance the radiation due to the asymmetric metal flares in the initial design. Fig. 5(b) first shows the influence on the reflection coefficients, where relatively stable results have been obtained. The E-plane radiation patterns at 72 GHz are shown in Fig. 5(c). It is seen that this parameter will alter the beam direction and gain. The gain difference can be as large as 2 dB, resulting from beam defocusing. A proper tradeoff should be performed for broadband operation.

B. FULL-WAVE SIMULATION RESULTS

One first considers a single antenna case. Based on the achieved optimum geometric parameters in Table 2, full-wave simulations by HFSS were performed to validate the feasibility. The achieved reflection coefficients are shown in Fig. 6(a), where some measurement results are also shown for later comparison in the next section. It is seen that the frequency range by full-wave simulations is 17-85 GHz (a

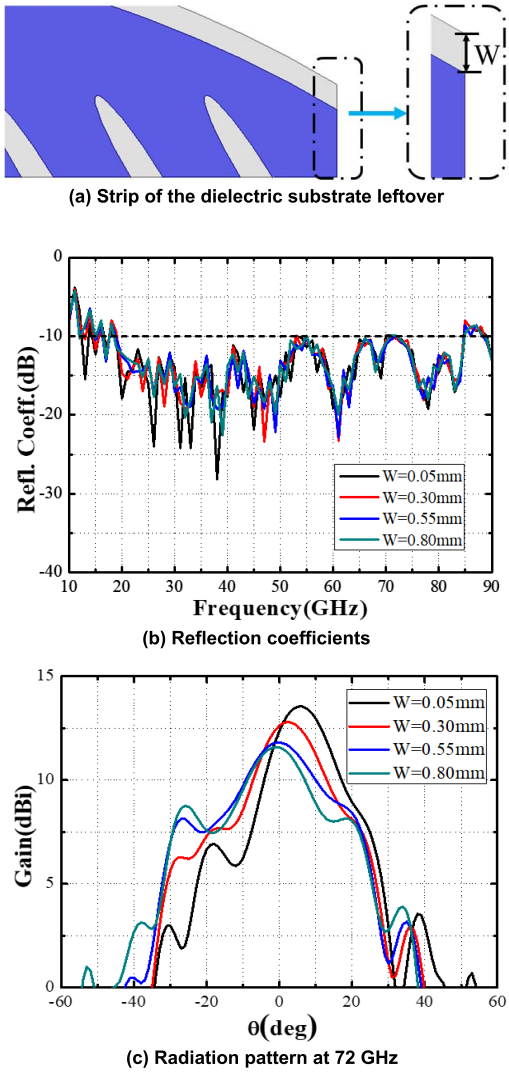

FIGURE 5. Parametric studies to the width of substrate cutout.

68 GHz bandwidth), or 133.3% fractional bandwidth with an up-down frequency ratio of 5. The gain performances and their corresponding antenna radiation efficiency are shown in Fig. 6(b). It is seen that the gains are larger than 10dB in most of the frequency bands. The maximum gain appears at 63 GHz by 13 dBi. However, they decrease from this maximum gain frequency at 63 GHz, remaining a relatively stable variation. The simulated efficiency is approximately 94%, which is relatively stable in the achieved band.

The beam squints are shown in Fig. 6(c), where the maximum deviation appears at low frequencies. In most of the frequency bands, the beam peak deviation is less than 3 degrees. The large beam squints at low frequencies do not cause difficulties because of their large beamwidths with tiny gain deviations for very small gain drops at low frequencies, as shown by the patterns in Fig. 7(a)-(d) at 28, 38, 60, and 72 GHz. These beam squints exist in the single antenna radiations, but their impacts will be reduced in an array situation because the array factor may lessen this effect. The XPLs in Fig. 8 are

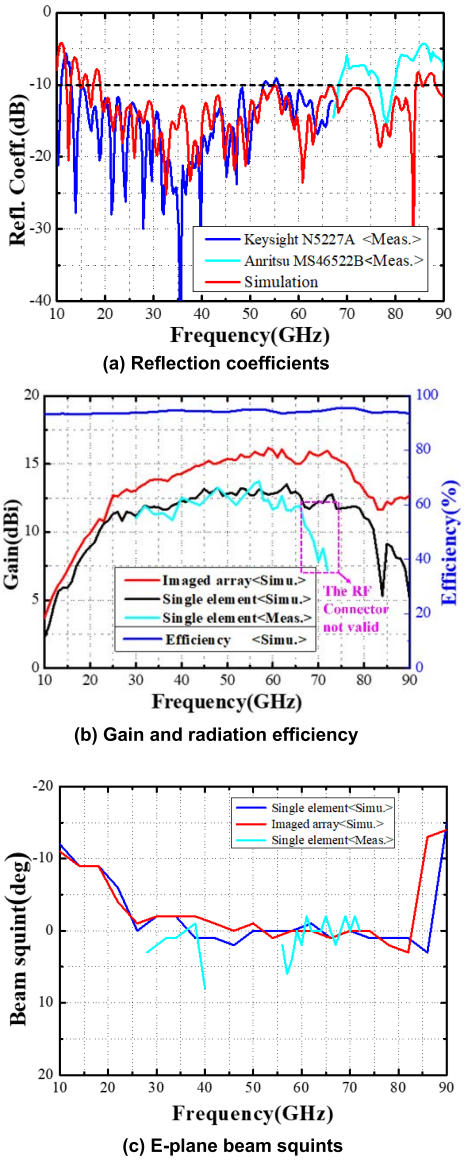

FIGURE 6. Summaries of reflection coefficients and radiation characteristics.

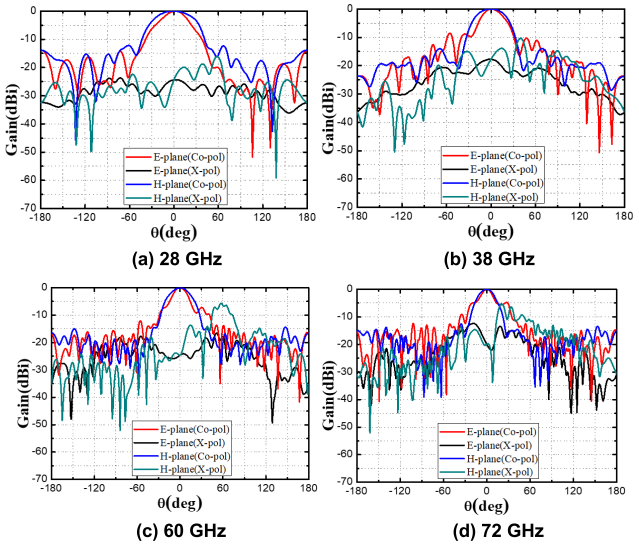

FIGURE 7. Simulated radiation patterns at 28, 38, 60, and 72 GHz.

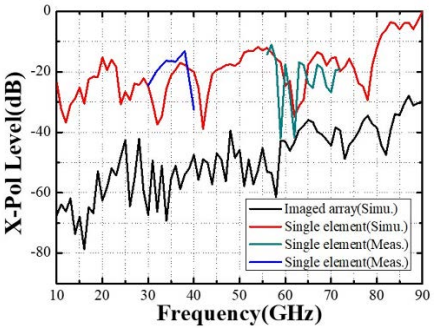

FIGURE 8. Comparing E-plane XPLs between the original and the paired BAVAs.

higher at high frequencies because the radiations arise from the structures near the feeding transition.

C. MIRROR-IMAGED ANTENNA PAIR

A mirror-imaged antenna architecture is formed to pair with the original antenna to demonstrate two purposes, as illustrated in Fig. 2, including beam squint impact reduction and XPL suppression on the E-plane. In this case, the separation is 6.25 mm, roughly 0.5λ at 24 GHz. This paired structure remains very compact, taking advantage of the low profile for each element. The former is achieved using the antenna array factor formed by the two antenna elements, which increases a 3dB gain in the broadside direction. On the other hand, the latter is achieved by producing two opposite X-pol directions from the mirror-imaged antenna architectures. In other words, the mirror-imaged architectures of the Vivaldi flares may well suppress the XPLs at low frequencies, which may not properly suppress the high-frequency XPLs because the major radiation parts of the antenna are very close to the feeding transition region to lose the symmetric natures. Indeed, such asymmetric structures near the feeding transition significantly produce X-pol components at mmW frequencies. The XPLs in [17] were approximately larger than -30dB and can be as large as -10dB for frequencies larger than 40 GHz. The measured results were even larger than -20dB toward -17dB at 40GHz.

The E-plane XPLs and beam squint comparisons between the original BAVA antenna and the paired ones are shown in Fig. 8 and Fig. 6(c), respectively. It is noted that, in principle, the X-pol components on the E-plane should be exactly canceled because they are in the opposite directions of equal magnitudes in the directional beam applications. It is seen from Fig. 8 that the XPLs in the paired antenna case are very low on the E-plane radiation patterns, which is much superior to the XPLs in the original antenna structure case. Moreover, the beam squint impact has also been improved, as seen by

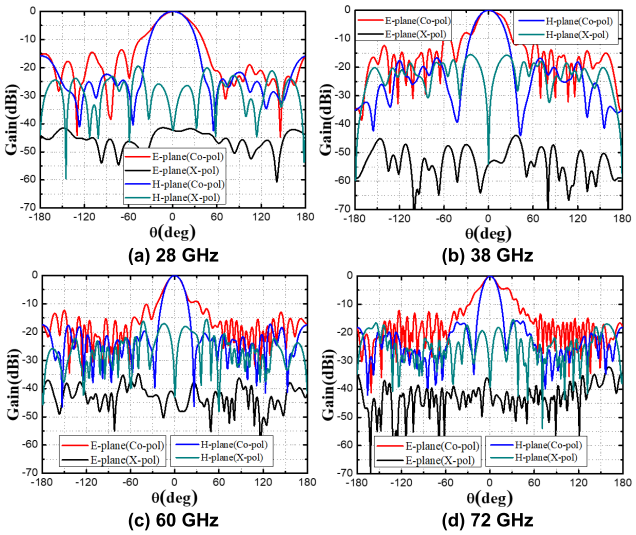

FIGURE 9. Simulated radiation patterns at 28, 38, 60, and 72 GHz for the paired BAVA.

the increase of gains in Fig. 6(b). The normalized E-plane radiation patterns at 28, 38, 60, and 72 GHz are shown in Fig. 9 (a)-(d), which show superior XPL behaviors on the E-plane patterns.

IV. EXPERIMENTAL VALIDATION

Experimental validation considers a single BAVA prototype, as shown in Fig. 10(a), which was measured in an anechoic chamber by the measurement setups in Fig. 10(b) and (c) at above 56 and below 40 GHz, respectively, based on their available valid frequency ranges. They are standard NSI-MI spherical and cylindrical antenna near-field (NF) scan systems, respectively. In the spherical scan system, a robotic arm is used to perform the great circle cut scan while the azimuth rotation is performed by the turn table to install the antennas. On the other hand, a vertical scanner is employed in the cylindrical scan system. The RF connector is a V-type end-launch connector of 1.85mm pin, whose operational band is limited to the frequency range below 67 GHz [26] with an estimation of maximum insertion loss of less than 0.3dB. Due to the broadband nature, the reflection coefficients were measured at different bands by several different network analyzers provided by Keysight and Anritsu. The radiation patterns were measured similarly. Thus, the results at frequencies larger than 67GHz are unreliable and are only used to show the trends.

The measured reflection coefficients are shown in Fig. 6(a) for easy comparison to the simulation results as expected that the results below 67 GHz agree very well with the simulation results. The lower frequency limit is extended to 13 GHz, as shown by the blue curve. On the other hand, the measurement at high frequencies is relatively complicated. The cable assembly is formed by integrating metal waveguides, coaxial cables, and the adaptors between them, which might cause fluctuations to the reflection coefficients because the adaptors are bandlimited. As mentioned earlier, the current

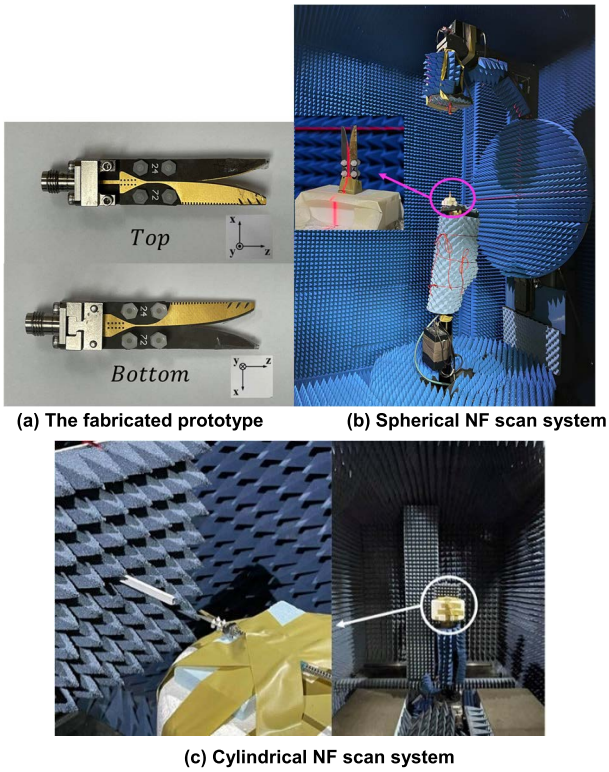

FIGURE 10. Antenna prototypes and measurement setup.

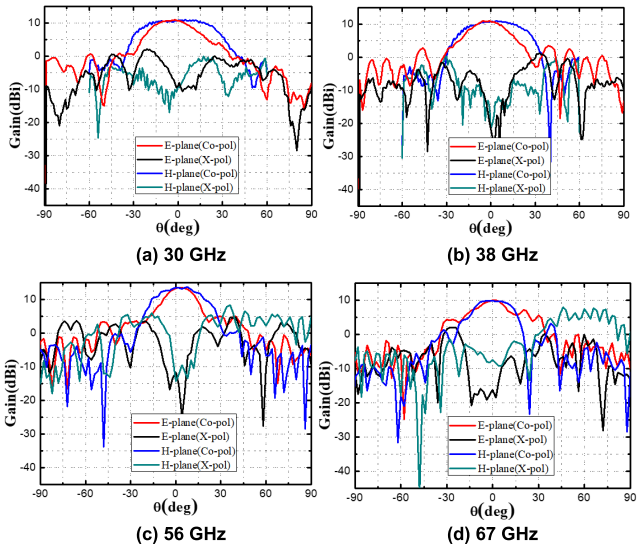

FIGURE 11. Measured radiation patterns at 30, 38, 56, and 67 GHz.

connector is limited to 67GHz. The reflection coefficients beyond 67 GHz are not accurate, which can be verified by the measured gains in Fig. 6(b). The gains drop very rapidly when the frequencies are larger than 67GHz. Based on these examinations, the valid frequency range is concluded to be 13-85GHz. The measured radiation patterns are shown in Fig. 11(a)-(d) at 30, 38, 56, and 67 GHz for reference. The difficulty of accurate position alignment causes high XPLs.

TABLE 3. Comparisons of similar BAVA designs ("A" indicates a frequency range of 20-85).

Ref.	Freq. Range (GHz)	Abs. BW (GHz)	Size (mm)	E-pl. XPL (dB)	ε_r	Subst. Thick. (mm)	Gain (dBi)	Max. Beam Dev. (deg)	Sim/Mea
[17]	10–40	30	79.9x24	-37~-24 (S) -31~-19 (M)	2.2	0.254	9.6–15	3°	S/M
[8]	6–20	14	76x56	--	2.5	1.5	9.4–12.1	10°	S
[9]	2.4–18	15.6	74x44	--	2.94	2.5	--	4°	S/M
[10]	1.5–15	13.5	140x70	-25	3.55	1.6	4.5–12.6	5°	S/M
[11]	3–18	15	96x50		2.55	1.57	4–13	9°	S/M
[13]	0.92-9.7	8.8	161.25x140	-25	2.33	3.15	3-10	N/A	S/M
[27]	1.8~6	4.2	98x84	-20	2.55	1	4-12	N/A	S/M
[28]	2.77-13.6	10.9	93x47	-25	3	0.762	15.2-24.6 (16 elements)	N/A	S/M
[29]	2-12	10			2.5			N/A	S
[30]	3.1-10.6	7.5	48x45.7	-20~-30	4.4	0.8	4.5-8.25	N/A	S/M
This work (single)	13-85	72	46.9x13	-40~-7	2.2	0.254	10-13 (A)	3° (A)	S/M
This work (pair)	13-85	72	46.9x13	-80~-34	2.2	0.254	12-16 (A)	3° (A)	S

Finally, a comparison of the characteristics with the reference BAVA designs in [8], [9], [10], [11], and [17] and the recent works in [13], [27], [28], [29], and [30] is given in Table 3. The proposed design's complete frequency range of 13–85 GHz appears to be the broadest. The size is also the most compact one. The XPL is also the smallest compared to these works. For a single BAVA, the E-plane XPL is the smallest at lower frequencies. At high frequencies, where the radiations from the feeding structures affect very much, the XPLs become worse, which impacts are reduced by the paired structure. The E-plane XPLs become $-80 \sim -34$ dB. It is noted that ideally, the XPLs of the paired antenna should be zeros because they should cancel exactly. The beam squints are less than 3 degrees for 20-85 GHz. It is larger at low frequencies, consistent with the reference works [8], [11]. The antenna pairing reduces the beam squint and XPL impacts at high frequencies.

V. CONCLUSION

This paper presents an improved BAVA structure for broadband operations from 13 to 85 GHz to cover various applications. The high-frequency radiation behaviors are examined to interpret the physical mechanism near the feeding structures. The design is achieved by relaxing the geometric constraints for more freedoms of optimization. The reached BAVA has a very broad bandwidth of reflection coefficients and low XPLs. The impacts of beam squints and the broad patterns on the cross-section dimension are reduced using the mirror-imaged antenna pair. Numerical full-wave simulations validate the design concept. Experimental validations were also performed at selected frequency bands where the measurements can be completed in the authors' facility. Good agreements with simulations have been achieved. Future works will pursue fabrication stability and wideband excitation validations.

REFERENCES

[1] S. A. Busari, S. Mumtaz, S. Al-Rubaye, and J. Rodriguez, "5G millimeter-wave mobile broadband: Performance and challenges," *IEEE Commun. Mag.*, vol. 56, no. 6, pp. 137–143, Jun. 2018.

[2] S. Xia, Q. Jiang, C. Zou, and G. Li, "Beam coverage comparison of LEO satellite systems based on user diversification," *IEEE Access*, vol. 7, pp. 181656–181667, 2019.

[3] A. Araghi, M. Khalily, P. Xiao, A. Kosari, H. Zarrabi, and R. Tafazolli, "Millimeter-wave MIMO balanced antipodal Vivaldi antenna design for autonomous cars," in *Proc. Int. Symp. Netw., Comput. Commun. (ISNCC)*, Jun. 2018, pp. 1–4.

[4] L. Qiao, Y. Wang, Z. Zhao, and Z. Chen, "Range resolution enhancement for three-dimensional millimeter-wave holographic imaging," *IEEE Antennas Wireless Propag. Lett.*, vol. 15, pp. 1422–1425, 2015.

[5] E. Gazit, "Improved design of the Vivaldi antenna," *IEE Proc. H Microw., Antennas Propag.*, vol. 135, no. 2, pp. 89–92, Apr. 1988.

[6] J. D. S. Langley, P. S. Hall, and P. Newham, "Novel ultrawide-bandwidth Vivaldi antenna with low cross-polarization," *Electron. Lett.*, vol. 29, no. 23, p. 2004, Nov. 1993.

[7] J. D. S. Langley, P. S. Hall, and P. Newham, "Balanced antipodal Vivaldi antenna for wide bandwidth phased arrays," *IEE Proc. Microw. Antennas Propag.*, vol. 143, no. 2, pp. 97–102, Apr. 1996.

[8] K. Kota and L. Shafai, "Gain and radiation pattern enhancement of balanced antipodal Vivaldi antenna," *Electron. Lett.*, vol. 47, no. 5, pp. 303–304, Mar. 2011.

[9] J. Bourqui, M. Okoniewski, and E. C. Fear, "Balanced antipodal Vivaldi antenna with dielectric director for near-field microwave imaging," *IEEE Trans. Antennas Propag.*, vol. 58, no. 7, pp. 2318–2326, Jul. 2010.

[10] L. Juan, F. Guang, Y. Lin, and F. Demin, "A modified balanced antipodal Vivaldi antenna with improved radiation characteristics," *Microw. Opt. Technol. Lett.*, vol. 55, no. 6, pp. 1321–1325, Jun. 2013.

[11] A. Molaei, M. Kaboli, S. A. Mirtaheri, and M. S. Abrishamian, "Dielectric lens balanced antipodal Vivaldi antenna with low cross-polarization for ultra-wideband applications," *IET Microw., Antennas Propag.*, vol. 8, no. 14, pp. 1137–1142, Nov. 2014.

[12] A. S. Dixit and S. Kumar, "A survey of performance enhancement techniques of antipodal Vivaldi antenna," *IEEE Access*, vol. 8, pp. 45774–45796, 2020.

[13] C. Sarkar, C. Saha, L. A. Shaik, J. Y. Siddiqui, and Y. M. M. Antar, "Frequency notched balanced antipodal tapered slot antenna with very low cross-polarised radiation," *IET Microw., Antennas Propag.*, vol. 12, no. 11, pp. 1859–1863, Sep. 2018.

[14] P. Wang, H. Zhang, G. Wen, and Y. Sun, "Design of modified 6–18 GHz balanced antipodal Vivaldi antenna," *Prog. Electromagn. Res.*, vol. 25, pp. 271–285, 2012.

[15] E. Guillanton, J. Y. Dauvignac, C. Pichot, and J. Cashman, "A new design tapered slot antenna for ultra-wideband applications," *Microw. Opt. Technol. Lett.*, vol. 19, no. 4, pp. 286–289, Nov. 1998.

[16] J. D. S. Langley, P. S. Hall, and P. Newham, "Novel ultrawide-bandwidth Vivaldi antenna with low crosspolarisation," *Electron. Lett.*, vol. 29, no. 23, pp. 2004–2005, Nov. 1993.

[17] N.-N. Wang, M. Fang, H.-T. Chou, J.-R. Qi, and L.-Y. Xiao, "Balanced antipodal Vivaldi antenna with asymmetric substrate cutout and dual-scale slotted edges for ultra-wideband operation at millimeter-wave frequencies," *IEEE Trans. Antennas Propag.*, vol. 66, no. 7, pp. 3724–3729, Jul. 2018.

[18] Z. Briqech, J. Robitaille, K. Bishyk, K. Abdo, D. Bhogal, and A. Sebak, "High gain antipodal tapered slot antenna with sine-shaped corrugation and Fermi profile substrate slotted cut-out for MMW 5G," in *Proc. Global Symp. Millim.-Waves (GSMM)*, Montreal, QC, Canada, 2015, pp. 1–3.

[19] T.-K. Chen and G. H. Huff, "Stripline-fed Archimedean spiral antenna," *IEEE Antennas Wireless Propag. Lett.*, vol. 10, pp. 346–349, 2011.
[20] R. Rimolo-Donadio, J. Supper, T.-M. Winkel, H. Harrer, and C. Schuster, "Analysis and mitigation of parasitic mode conversion for microstrip to stripline transitions," *IEEE Trans. Electromagn. Compat.*, vol. 54, no. 2, pp. 495–498, Apr. 2012.
[21] Z. Yin, G. He, X. Yang, and S. Gao, "Miniaturized ultrawideband half-mode Vivaldi antenna based on mirror image theory," *IEEE Antennas Wireless Propag. Lett.*, vol. 19, no. 4, pp. 695–699, Apr. 2020.
[22] S. Yun, D. Y. Kim, and S. Nam, "Bandwidth enhancement of cavity-backed slot antenna using a via-hole above the slot," *IEEE Antennas Wireless Propag. Lett.*, vol. 11, pp. 1092–1095, 2012.
[23] F. X. Che and Z. Chen, "Study on electrical performance and mechanical reliability of antenna in package (AIP) with fan-out wafer level packaging technology," in *Proc. IEEE 20th Electron. Packag. Technol. Conf. (EPTC)*, Singapore, Dec. 2018, pp. 180–185.
[24] D. Liu, X. Gu, C. W. Baks, and A. Valdes-Garcia, "Antenna-in-package design considerations for Ka-band 5G communication applications," *IEEE Trans. Antennas Propag.*, vol. 65, no. 12, pp. 6372–6379, Dec. 2017.
[25] D. A. Hill, D. G. Camell, K. H. Cavcey, and G. H. Koepke, "Radiated emissions and immunity of microstrip transmission lines: Theory and reverberation chamber measurements," *IEEE Trans. Electromagn. Compat.*, vol. 38, no. 2, pp. 165–172, May 1996.
[26] *RF Connector*. Accessed: Dec. 5, 2021. [Online]. Available: http://www.bojiang.com.tw/en/product/1092.html
[27] K. Zhang, R. Tan, Z. H. Jiang, Y. Huang, L. Tang, and W. Hong, "A compact, ultrawideband dual-polarized Vivaldi antenna with radar cross section reduction," *IEEE Antennas Wireless Propag. Lett.*, vol. 21, no. 7, pp. 1323–1327, Jul. 2022.
[28] F. Abushakra, N. Jeong, A. K. Awasthi, and S. Kolpuke, "Ultra-wideband coplanar Vivaldi antenna array with dielectric patch antenna for grating lobes suppression," *IEEE Access*, vol. 10, pp. 54410–54420, 2022.
[29] P. Mahouti, A. Kızılay, O. Tari, A. Belen, and M. A. Belen, "Design optimization of ultra wide band Vivaldi antenna using artificial intelligence," in *Proc. Int. Appl. Comput. Electromagn. Soc. Symp. (ACES)*, 2021, pp. 1–4.
[30] S. Guruswamy, R. Chinniah, and K. Thangavelu, "Design and implementation of compact ultra-wideband Vivaldi antenna with directors for microwave-based imaging of breast cancer," *Analog Integr. Circuits Signal Process.*, vol. 108, pp. 45–57, May 2021.

HSI-TSENG CHOU (Fellow, IEEE) received the B.S. degree in electrical engineering from the National Taiwan University, Taiwan, in 1988, and the M.S. and Ph.D. degrees in electrical engineering from The Ohio State University (OSU), in 1993 and 1996, respectively.

He joined the ElectroScience Laboratory (ESL), OSU, as a Graduate Research Associate, during 1991–1996, and as a Postdoctoral Researcher, during 1996–1998. He is currently appointed as a Distinguished Professor with the Graduate Institute of Communication Engineering and the Department of Electrical Engineering, National Taiwan University. He has published more than 550 journals and conference papers, and holds 50 patents. His research interests include wireless communication networks, antenna design, antenna measurement, electromagnetic scattering, and asymptotic high-frequency techniques, such as uniform geometrical theory of diffraction (UTD), novel Gaussian beam techniques, and UTD type solution for periodic structures.

Dr. Chou is an IET Fellow. He is an Elected Member of the URSI International Radio Science U.S. Commission B. He has received many awards to recognize his distinguished contributions in the technological developments. Some important ones includes a Distinguished Contribution Award in promoting inter- academic and industrial cooperation from the Ministry of Education, a Distinguished Engineering Professor Award from the Chinese Institute of Engineers, a Distinguished Electrical Engineering Professor Award from the Chinese Institute of Electrical Engineering, the University's Industrial Economics Contribution Award from the Ministry of Economics in 2008, the National Industrial Innovation Awards—Key Technology Elite Award from the Ministry of Economics in 2011, and the Industrial-Academia Collaboration Award from the Ministry of Economics in 2017. His work in active antenna calibration was awarded by the Ministry of Science and Technology, Taiwan, as the "Future Technology Award," in 2020. He received the Best Chapter Award in 2012. He was elected in 2004 as one of the Nation's Ten Outstanding Young Persons by Junior Chamber International, the National Young Person Medal from China Youth Corps of Taiwan in 2005, and as one of the top ten rising stars in Taiwan by the Central News Agency of Taiwan. He also received Outstanding Branch Counselor Awards from IEEE, including IEEE Headquarter, R-10, and Taipei Section, respectively. He received the IEEE Technical Field Undergraduate Teaching Award in 2014. He has served as the Chair for the IEEE AP-S Taipei Chapter. He served as the Chair for the EMC-S Taipei Chapter during 2019–2021.

YEN-JU LIN was born in Pingtung, Taiwan, in 1997. He received the B.S. degree in electrical engineering from Feng Chia University, in 2019, and the M.S. degree from the Graduate Institute of Communication Engineering, National Taiwan University, Taiwan, in 2021. He is currently an Antenna Research and Development Engineer with MediaTek Inc. His research interests include antenna-in-package (AiP) and broadband antennas at millimeter-wave (mmW) frequencies for mobile communications.